nature communications

Article

https://doi.org/10.1038/s41467-025-67537-3

Krypton/Xenon separation at room temperature in a flexible coordinative framework sorbent

Received: 4 July 2025

Accepted: 3 December 2025

Published online: 26 January 2026

Check for updates

Siqi Dong[1,5], Bochun Zhang[2,5], Mohammad Wahiduzzaman[3], Chuting Yang[1], Qiang Liu[1], Guillaume Maurin[3,4], Shunshun Xiong[1] ✉, Sujing Wang[2] ✉ & Xiaolin Wang[1] ✉

The separation of xenon from krypton holds significant importance across various fields, including high-tech industries, national defence, and aerospace. Adsorptive separation via porous solids is considered one of the most promising alternatives to conventional energy-intensive cryogenic processes. While traditional adsorbents selectively capture xenon over krypton under ambient conditions, their desorption energy penalties for producing pure xenon impede practical implementation. Here, we present a metal–organic framework characterized by synergistic structural and local flexibility that reverses conventional selectivity, thereby enabling preferential adsorption of krypton at room temperature. This material demonstrates a krypton uptake of 36.8 $cm^3 cm^{-3}$ (298 K, 1 bar) and achieves a Kr/Xe selectivity of 10.4 in 1/99 Kr/Xe mixture breakthrough experiments. Moreover, this material exhibits commendable radioactive stability and effectively captures trace amounts of krypton (40 ppm). Mechanistic studies indicate that dynamic adjustments in cavity windows and localized ligand vibrations work synergistically to exploit subtle size differences between krypton and xenon. This enables kinetically controlled sieving of krypton through transiently expanded channels. With an energy-efficient approach to krypton-centric separation, our research redefines the design paradigm for noble gas purification and offer new possibilities for separating other dynamically matched molecules through adaptive host–guest interactions.

Xenon (Xe) is a highly valuable noble gas that is experiencing increasing demand across various high-tech industries, medical therapies, national defences, aerospace, nuclear energy, fundamental research, and even everyday applications[1–5]. While air serves as a primary source for Xe production through energy-intensive cryogenic processes, exhaust gases from the nuclear sector also represent an important alternative[6,7]. In both scenarios, krypton (Kr) is present at varying concentrations and must be effectively removed from the Xe/Kr mixture. Consequently, the cost-effective and energy-efficient separation of Xe from Kr is essential to meet the growing market demand for Xe across diverse applications.

With significant advancements in purification technologies, the adsorptive separation of Xe/Kr using porous solids has become a promising alternative to conventional methods[8–10]. However, the comparable sizes of Xe (4.047 Å) and Kr (3.655 Å) make size-selective molecular sieving challenging for most porous materials. These

[1]Institute of Nuclear Physics and Chemistry (INPC), China Academy of Engineering Physics (CAEP), Mianyang, China. [2]Hefei National Research Center for Physical Sciences at the Microscale, Laboratory of Spin Magnetic Resonance, Suzhou Institute for Advanced Research, Hefei National Laboratory, University of Science and Technology of China, Hefei, China. [3]ICGM, Univ. Montpellier, CNRS, ENSCM, Montpellier, France. [4]Institut Universitaire de France, Paris, France. [5]These authors contributed equally: Siqi Dong, Bochun Zhang. ✉e-mail: ssxiong@caep.cn; sjwang4@ustc.edu.cn; xlwang@caep.cn

solids typically favor thermodynamic Xe-selective adsorption because of their higher polarizability (40.44×10^{-25} cm^3) than Kr (24.84×10^{-25} cm^3)[11,12]. While some Xe-selective adsorbents can achieve selectivity greater than 100, producing high-purity Xe still requires considerable energy because preferentially adsorbed Xe must be desorbed for recovery[13–16]. Additionally, capturing low concentrations of radioactive ^{85}Kr isotopes (40 ppm), which have a long half-life of 10.8 years and are found in nuclear exhaust gases, is crucial to minimize environmental impact[6,17,18]. Rapid sequestration and transfer of this isotope to storage facilities are essential. To facilitate the direct recovery of pure Xe during adsorption, Kr must be preferentially adsorbed through a kinetic-driven sieving mechanism.

To date, only a few porous materials can sieve Kr from Xe: the densified CuBTC to form FS-CuBTC$_{UM}$ sorbent[19], the porous carbon C-Suc-750 material with an appropriate pore size of approximately 4.0 Å[20] and three MOFs, i.e., FMOFCu, Mn(ina)$_2$ and CoNi-DAB with attractive separation performance at low temperatures below 273 K through kinetic-controlled molecular sieving[21–23] (Fig. 1a). In addition to inherent local flexibility like bond rotation and stretching, guest-responsive dynamic MOF frameworks with narrow pore windows show promise in distinguishing between these gases due to significant differences in diffusion energy through small apertures[24–26]. These findings suggest that fine-tuning structural flexibility and pore size in this class of porous materials could enable selective Kr adsorption at room temperature via kinetic-controlled sieving.

Herein, we demonstrate the preferential adsorptive separation of Kr over Xe at room temperature using the ultrasmall-pore MOF MIP-203-Suc (developed by the Institute of Porous Materials in Paris and based on succinic acid)[27]. This zirconium MOF exhibits synergistic structural flexibility with temperature- and guest-responsive dynamics, as well as local bond rotation and stretching (Fig. 1b). Thermal activation induces notable pore shrinkage, creating optimal apertures for Kr/Xe separation. The inherent flexibility of the aliphatic chain in succinate further fine-tunes accessibility to Kr and Xe. We observe a significant difference in the diffusion energy barriers: 12.8 kJ mol^{-1} for Kr versus 21.0 kJ mol^{-1} for Xe, indicating a strong kinetic preference for Kr transport through the narrow pores of MIP-203-Suc. This molecular discrimination results in excellent separation performance, confirmed by breakthrough experiments with a 1/99 Kr/Xe mixture at room temperature, yielding a selectivity factor of 10.4. In addition to its kinetic-controlled sieving capabilities, MIP-203-Suc shows excellent Kr uptake of 36.8 cm^3 cm^{-3} from single-component sorption isotherms. Notably, this MOF maintains its separation efficacy across various Kr/Xe ratios, facilitating high-purity Xe production. Furthermore, it demonstrates exceptional trace-capture ability by selectively removing Kr even at concentrations as low as 40 ppm from Xe-rich mixtures typical of nuclear reprocessing off-gases.

Results

Temperature-driven pore structure transition and single-gas sorption isotherms

To achieve kinetic-driven sieving of Kr over Xe through adsorptive separation, it is essential to use porous materials with precisely sized and shaped pore apertures that can effectively distinguish the subtle dimensional differences between Kr and Xe. This requires the development of highly ordered porous frameworks with exceptional pore size control. Conventional inorganic porous solids, such as modified oxides and porous carbons, often have broad pore size distributions, making them unsuitable for this application. Additionally, the local flexibility of microporous MOFs with well-ordered pores significantly aids in the selective adsorption of Kr over Xe under cryogenic conditions[21–23]. These insights help identify MOF materials capable of achieving Kr/Xe separation at room temperature. Our comprehensive examination led us to explore MIP-203-Suc, a zirconium-based MOF made from 10-coordinated Zr_6 clusters and succinate linkers featuring an inherently flexible C4 backbone. This framework combines optimal

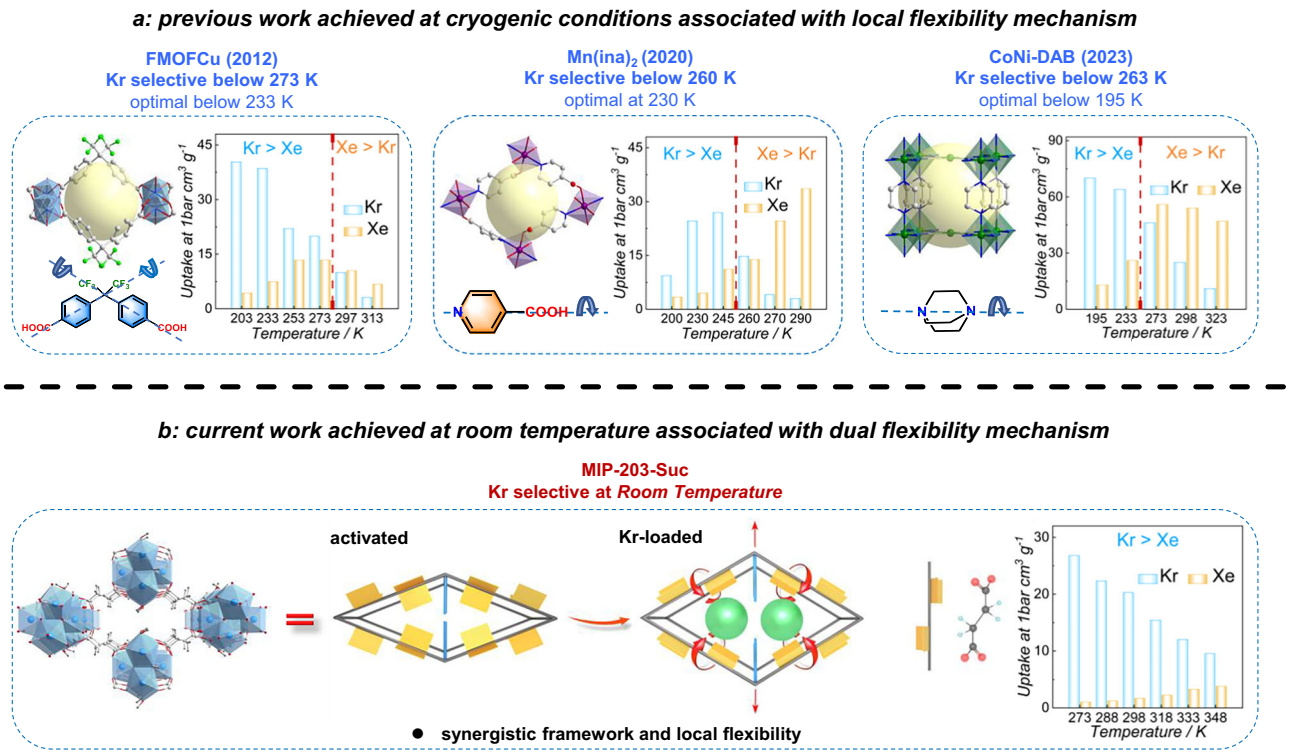

Fig. 1 | Strategies for achieving the selective adsorption of Kr over Xe. a Previous studies documented in the literature, including three examples to date, have been associated with the mechanism of linker rotation-induced local flexibility observed under cryogenic conditions (temperatures below 273 K). Notably, all three materials selectively adsorb Xe over Kr at room temperature. **b** Current work associated with synergistic framework dynamics and local flexibility observed at room temperature.

pore dynamics and local flexibility[27], making it highly suitable for room-temperature Kr/Xe separation.

The reduced connectivity of Zr_6 clusters in MIP-203-Suc (10-connected versus 12-connected in rigid analogues) enhances framework flexibility. This structural adaptability stems from lower node connectivity, promoting greater ligand mobility and dynamic responses to external stimuli. The as-synthesized structure of MIP-203-Suc, modeled via density functional theory (DFT) geometry optimization and powder X-ray diffraction (PXRD) data[27], exhibits anisotropic modulation of pore apertures upon thermal activation at 373 K. Along the *a*-axis of the crystal structure, the effective window size, estimated from the carbon–carbon distance between succinate ligands on neighboring Zr_6 clusters within the 1D channels, considering the van der Waals radii of carbon atoms (2 × 1.7 Å), shrinks from 4.1 Å (in the as-synthesized structure) to 3.7 Å upon thermal activation. Conversely, the aperture along the *b*-axis expands slightly from 2.5 to 2.8 Å after activation (Fig. 2a and b, Supplementary Table 1), indicating anisotropic stress relaxation via ligand reorientation along different crystallographic directions.

To validate the permanent porosity of activated MIP-203-Suc, CO_2 adsorption measurements were conducted at 195 K (Supplementary Fig. 3), yielding a Brunauer-Emmett-Teller (BET) area of 161 $m^2 g^{-1}$. Pore size distribution analysis employing the Horvath-Kawazoe (H-K) method revealed bimodal characteristics with peaks centered at about 4.0 Å and 5.0 Å (Supplementary Fig. 4). These pore dimensions are consistent with the crystallographically resolved one-dimensional channels composed of bottle-shaped cavities along the a-axis direction. While static structures have constrained pores, succinate linker flexibility through torsional motion is expected to facilitate dynamic aperture adaptation during gas diffusion, potentially enabling kinetic Kr/Xe separation through kinetically controlled sieving. Specifically, transient narrowing of pore apertures along the *a*-axis may preferentially restrict larger Xe atoms while allowing faster permeation of smaller Kr atoms—even when equilibrium adsorption selectivity favors Xe.

To assess the efficacy of the activated MIP-203-Suc sample in selectively adsorbing Kr from Xe and other gases, initial single-component sorption measurements were conducted (Supplementary Fig. 5). The corresponding results were subsequently plotted against volumetric uptake, as the volumetric adsorption capacity is commonly utilized when different sorbents with varying densities are compared in practical applications[13]. The Kr isotherms collected at temperatures above 268 K exhibit a standard decrease in the adsorption amount and a weaker affinity as the temperature increases (Fig. 3a). This behavior aligns with that observed for other gases, where the aperture size of the porous materials does not limit the entrance of guest molecules[26,28–30]. However, the Kr uptake decreased as the measurement temperature dropped below 268 K, this observation is in line with the flexible nature of the activated MIP-203-Suc structure: a significant steric hindrance due to limited bond stretching and rotation at low temperature impedes Kr to enter into the pore structure, resulting in a decreased Kr adsorption uptake (Fig. 3b). Notably, the Kr uptake observed in MIP-203-Suc at 298 K and 1 bar (36.8 $cm^3 cm^{-3}$) ranks among the highest values reported to date for porous materials (Fig. 3d), substantially surpassing some Xe-selective materials, such as Ag-MOF-303[31], $Co_3(HCOO)_6$[32], HOF-FJU-46[33] and CC3[34]. However, owing to the rather small pore volume of MIP-203-Suc, its Kr uptake is slightly lower than that of MOFs with larger pore volumes, such as MOF-Cu-H[18] and ZJU-74a-Pb[14] (Supplementary Table 4).

As for the Xe adsorption isotherms, MIP-203-Suc exhibited an inverse trend in uptake with temperature under the same testing conditions. When the temperature increases, local flexibility within the succinate linkers becomes increasingly pronounced; this notably enhances the ability to permit Xe passage through confined pore windows, thereby leading to significantly increased Xe uptake at elevated temperatures, such as those observed at 348 K (Fig. 3b and Supplementary Fig. 6). Consequently, across the temperature range from 253 to 348 K, Kr uptake consistently surpasses that of Xe by a substantial margin, suggesting an excellent separation performance of this material for Kr over Xe. In comparison to the previously reported MOFs, i.e., FMOFCu[21], $Mn(ina)_2$[22], and CoNi-DAB[23], MIP-203-Suc demonstrates a broader sieving temperature range and superior Kr/Xe uptake ratio (Supplementary Fig. 7). Other molecules present in air, such as argon (Ar), oxygen (O_2), and nitrogen (N_2), exhibit negligible adsorption uptakes (Fig. 3c). These findings highlight the significant potential of activated MIP-203-Suc for selectively adsorbing Kr. In view

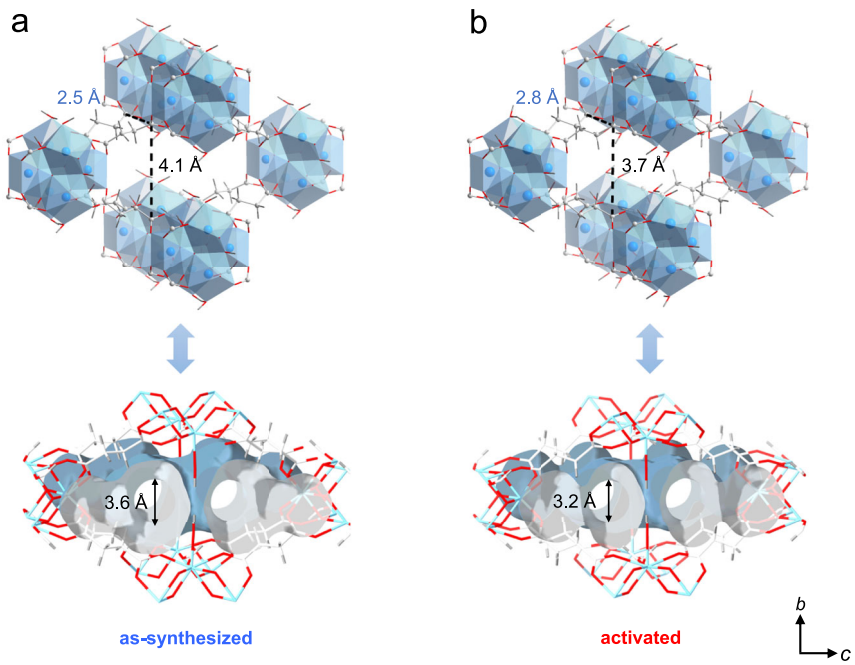

Fig. 2 | Crystal structures of MIP-203-Suc. a, b Description of axial structural change and Connolly surface for as-synthesized and activated MIP-203-Suc. Zr, blue; C, white; O, red; H, gray.

https://doi.org/10.1038/s41467-025-67537-3

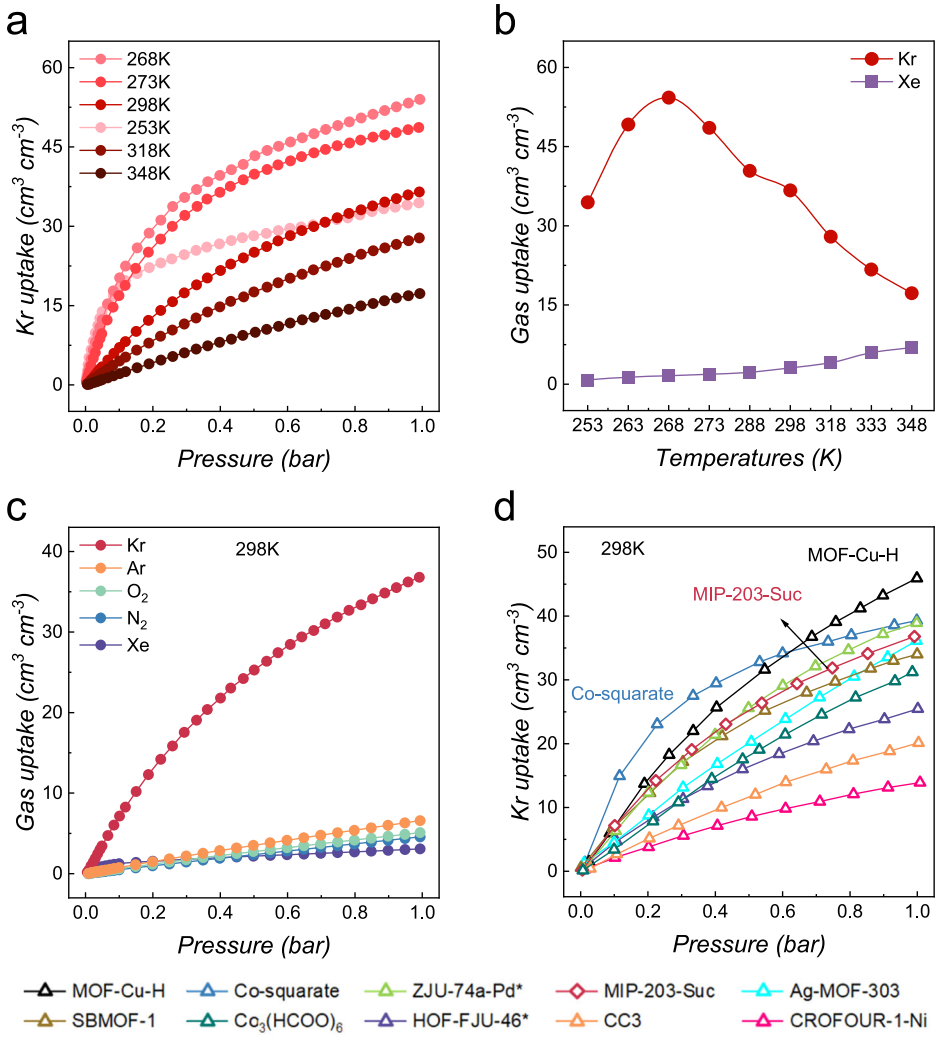

Fig. 3 | Single-component gas sorption on activated MIP-203-Suc and its comparison with other benchmark sorbents. a Krypton adsorption isotherm for activated MIP-203-Suc samples collected at various temperatures. **b** Correlation plots between the Xe and Kr uptake at 1 bar and the indicated temperatures. **c** Comparative analysis of the adsorption isotherms for krypton, argon, oxygen, nitrogen, and xenon at 298 K. **d** Comparison of krypton adsorption isotherms and uptake capacities between activated MIP-203-Suc and other representative porous materials. *: Data acquired at 296 K.

of the anomalous temperature-changes of the Xe and Kr adsorption uptakes of MIP-203-Suc, the temperature-dependent pore structural flexibility and the corresponding temperature-dependent diffusion processes of Xe or Kr within the narrow pore apertures in MIP-203-Suc are likely the main causes. Therefore, we pursued further investigation into the kinetic adsorption performance of Kr and Xe on MIP-203-Suc. As shown in Supplementary Figs. 8–10, the diffusion time constants and kinetic selectivity of Xe and Kr on MIP-203-Suc were calculated using the classical micropore diffusion model[35]. The diffusion time constants were calculated to be 7.38×10^{-4} min^{-1} for Xe and 9.37×10^{-3} min^{-1} for Kr at 298 K and 50 kPa, indicating a notably faster diffusion rate of Kr relative to Xe and yielding a high kinetic Kr/Xe selectivity of 12.7. Temperature-dependent diffusion studies reveal that, at 1 kPa, the diffusion time constants of Xe at 273 K (3.44×10^{-4} min^{-1}) increased significantly to 6.13×10^{-4} min^{-1} at 298 K and 8.77×10^{-4} min^{-1} at 318 K. While for Kr at the same pressure, it only slightly increased from 1.72×10^{-3} min^{-1} at 273 K to 2.03×10^{-3} min^{-1} at 298 K. The increase in temperature can enhance the molecular diffusivity and adsorption kinetics, with Xe exhibiting substantially stronger temperature-responsive behavior compared to Kr. This confirms the theoretical expectation that larger molecular gases are more sensitive to thermal activation due to their higher intrinsic diffusion barriers.

Breakthrough experiments and kinetic-driven sieving mechanism

To evaluate the dynamic separation performance of MIP-203-Suc, we conducted breakthrough experiments utilizing an equimolar Kr/Xe mixture. The gas mixture was introduced into a packed column containing the activated sorbent at 298 K, with a constant flow rate of 1.5 mL min^{-1} (Fig. 4a and Supplementary Fig. 11). Consistent with the results of preliminary single-component adsorption measurements, a distinct separation of the Kr/Xe mixture was observed. Pure Xe eluted first from the column at approximately 5 minutes, while Kr remained for approximately 15 min. Following this period, Kr began to break through and approached equilibrium conditions by approximately 90 minutes. The robust regeneration and cycling capabilities of MIP-203-Suc were demonstrated through five consecutive breakthrough cycles conducted under identical conditions (Supplementary Fig. 12). The dynamic adsorption capacity of Kr on MIP-203-Suc, as determined from the breakthrough curve, was calculated to be 0.40 mmol g^{-1}. This value is slightly lower than the corresponding equilibrium uptake derived from the adsorption isotherms (0.62 mmol g^{-1}), which is likely due to mass transfer limitations and the relatively slow diffusion of Kr into the MOF pores under dynamic conditions. Notably, the selectivity for Kr/Xe obtained from these breakthrough experiments reached a

https://doi.org/10.1038/s41467-025-67537-3

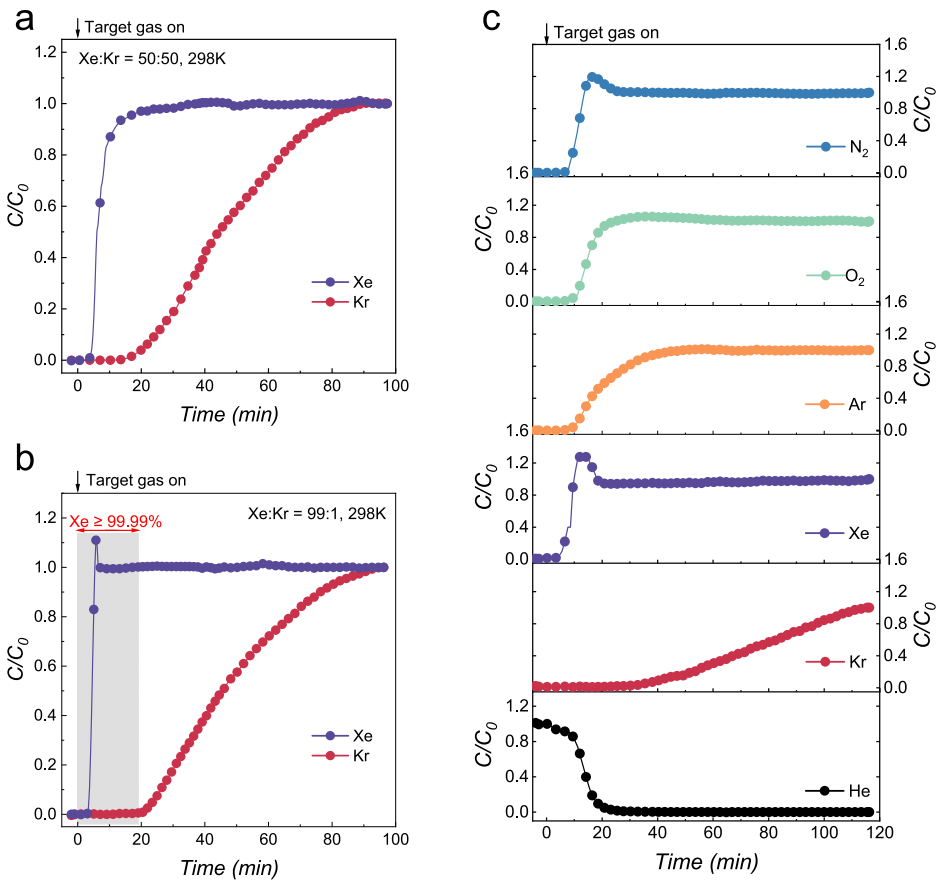

Fig. 4 | Kr/Xe dynamic separation by MIP-203-Suc. a Column breakthrough curves of activated MIP-203-Suc at 298 K for mixtures of Kr/Xe (50/50 vol%). **b** Column breakthrough curves of activated MIP-203-Suc at 298 K for the mixed gases of Kr/Xe (1/99 vol%). **c** Column breakthrough results of activated MIP-203-Suc at 298 K for a simulated exhaust gas mixture (400 ppm Xe, 40 ppm Kr balanced with dry air).

value of 6.3 at room temperature, underscoring the exceptional capacity of the material for kinetically controlled sieving (Supplementary Note 2).

With the dynamic Kr selectivity of MIP-203-Suc established, we subsequently evaluated its capacity for Xe purification from trace Kr contaminants through a breakthrough experiment utilizing a 99:1 Xe/Kr mixture to simulate relevant conditions. As illustrated in Fig. 4b, Xe eluted from the packed column in less than 5 min, whereas Kr was retained for more than 22 min, demonstrating the exceptionally high selective behavior of MIP-203-Suc under trace-level separation conditions. This process resulted in post treated Xe gas with significantly enhanced purities exceeding 99.99%, as determined by chromatography data (Supplementary Figs. 14 and 15). Consequently, the purity of Xe can be increased by a factor of 100 (from 99 to 99.99%) within a single cycle of dynamic separation at room temperature, effectively removing trace amounts of Kr—an outcome that holds considerable promise for practical applications. Notably, the calculated Kr/Xe selectivity under these conditions reaches 10.4 at room temperature, representing a 65% increase compared with the value obtained from a Kr/Xe mixture with a ratio of 50:50 (Supplementary Note 2).

Furthermore, to address the urgent challenge of rapidly removing radioactive Kr isotopes from exhaust gases produced by nuclear industrial waste, a simulated mixture of nuclear exhaust gases—comprising 400 ppm Xe and 40 ppm Kr—was subjected to dynamic separation testing. As illustrated in Fig. 4c and Supplementary Fig. 16, Xe is eluted from the column first, followed by argon (Ar), nitrogen (N_2), and oxygen (O_2). Notably, Kr remains trapped within the column for up to 32 min before breakthrough occurs, underscoring the exceptional trapping efficiency of MIP-203-Suc in dilute separation regimes, with an extraction rate of 0.054 mmol kg^{-1} Kr from simulated nuclear exhaust gas streams. Importantly, this material retains its structural integrity and superior separation performance under γ-irradiation at doses up to 100 kGy (Supplementary Figs. 17–19). This advancement signifies substantial potential for the reprocessing of nuclear off-gas streams.

To elucidate the kinetics-driven sieving mechanism of the activated MIP-203-Suc material and its guest-induced structural response, we integrated advanced DFT simulations with comprehensive experimental characterization. The energy barriers for Kr and Xe diffusion through the pore apertures of the activated MIP-203-Suc were computed via DFT-based climbing-image nudged elastic band (CI-NEB) calculations. The central ellipsoidal porosity of MIP-203-Suc connects to eight triangular apertures along the crystallographic *a*- and *b*-axes, with two bridging formates contributing to an asymmetric pore landscape (Supplementary Note 4 and Supplementary Fig. 20). Depending on their orientations, these bridging formates induce a distortion of the central porosity into an asymmetrical ellipsoidal cage where one side, along with its corresponding apertures, becomes significantly narrower than the other side of the Zr_6 cluster (Supplementary Tables 1 and 2). All crystallographic possible pathways were systematically identified, leading to eight potential diffusion pathways, with only six are geometrically viable (Supplementary Note 5 and Supplementary Fig. 21).

Along the *a*-axis, four diffusion paths traverse triangular apertures framed by succinate linkers and terminal OH-H_2O groups of Zr_6 clusters. These paths organize into two geometrically distinct pairs (Path-

https://doi.org/10.1038/s41467-025-67537-3

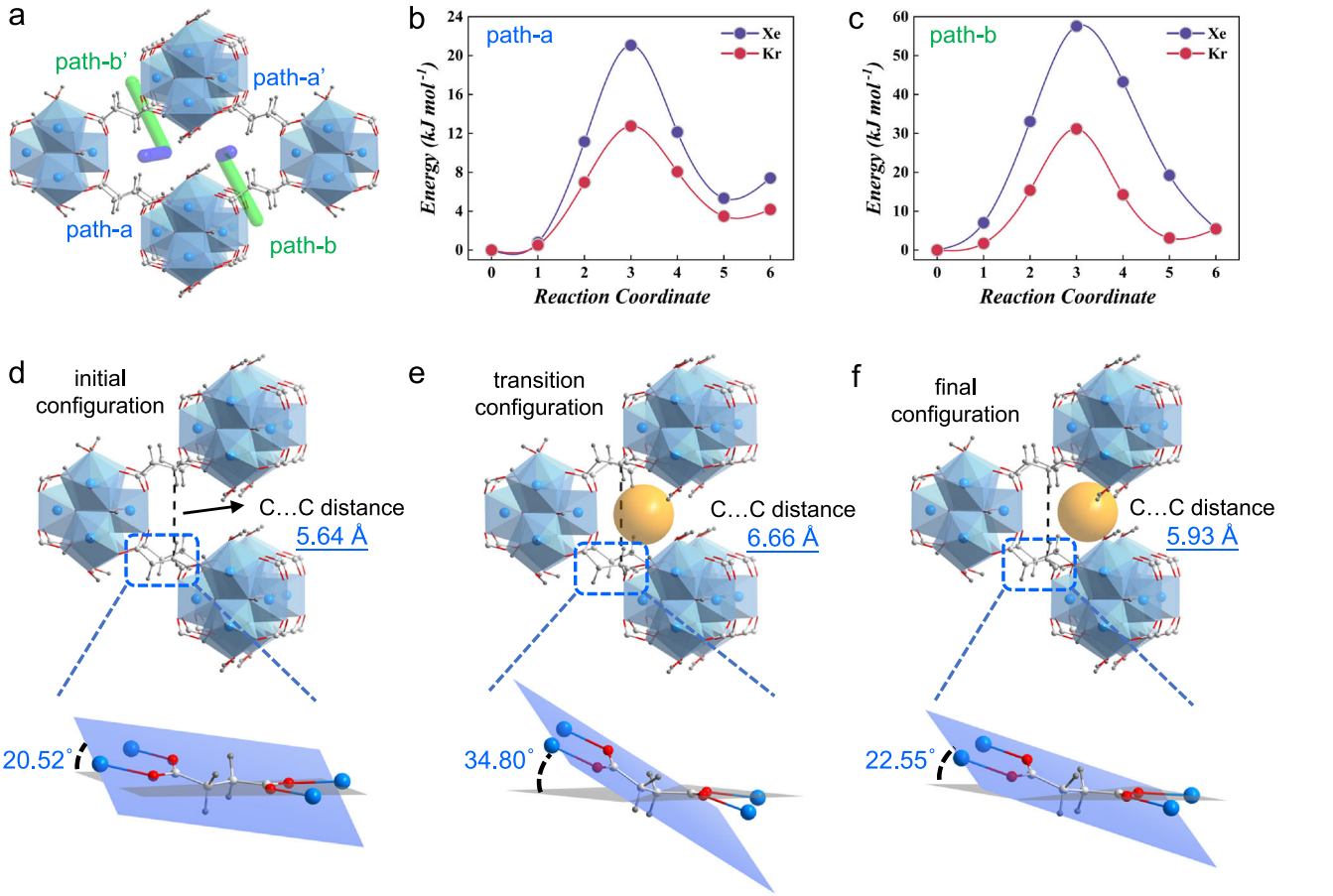

Fig. 5 | Kinetically driven sieving mechanism of Kr over Xe in the activated MIP-203-Suc structure. a Two possible guest diffusion pathways, referred to as Path-a and Path-b, are illustrated along the crystallographic *a*- and *b*-axes throughout the pore apertures of the activated MIP-203-Suc structure. **b** DFT-simulated minimum energy paths (MEPs) for Kr and Xe along Path-a. **c** DFT-simulated MEP for Kr and Xe along Path-b. Structural details of the MOF window pore opening along Path-a **d** Prior to Kr crossing (initial configuration), **e** During Kr pore window crossing (transition configuration), and **f** once Kr reaches the pore (final configuration). Zr, blue; C, white; O, red; H, gray; Kr, orange.

a/Path-a') with different aperture dimensions (C–C (2nd C in the aliphatic chain) distance = 5.64 Å vs 4.70 Å; Supplementary Table 2) on opposing sides of the Zr_6 clusters. Given this measurable geometric disparity, we analysed one path from each size category (Path-a and Path-a') to capture the full range of *a*-axis diffusion behavior. The *b*-axis shows even greater heterogeneity. While four potential routes exist, synergistic occlusion by bridging formates CH wedges, and adjacent succinate linkers sterically block Path-b2 and Path-b2' (Supplementary Fig. 22; Supplementary Videos 1 and 2). The remaining Path-b and Path-b' retain viable diffusion channels with significant aperture differences (5.4 Å vs. 4.2 Å; Supplementary Table 2). Therefore, four distinct paths were investigated to characterize the entire framework's anisotropic diffusion landscape.

The CI-NEB-calculated minimum energy paths (MEPs) reveal significant differences in the migration behavior of the two guest molecules. Along the crystallographic *a*-axis, Path-a (Fig. 5a) exhibited moderate energy barriers of 12.8 kJ mol^{-1} for Kr and 21.0 kJ mol^{-1} for Xe, i.e., $\Delta E_{Xe\text{-}Kr} \approx 8$ kJ mol^{-1} (Fig. 5b and Supplementary Videos 3 and 4). As anticipated, the asymmetric pore architecture creates distinct diffusion environments even among structurally related pathways. For example, Path-a', with a slightly narrower constriction of 4.7 Å (separating the distance between the second carbons in the aliphatic chains along the *a*-axis, vs. 5.64 Å for Path-a (see illustration in Fig. 5d)) increases the energy barriers to 33.1 kJ mol^{-1} for Kr and 43.8 kJ mol^{-1} for Xe, resulting in a $\Delta E_{Xe\text{-}Kr}$ of ~11 kJ mol^{-1} (Supplementary Fig. 23). Diffusion along the *b*-axis through Path-b and Path-b' results in a significantly tighter constriction formed by succinate linkers and bridging formates, resulting in substantially higher energy barriers: 31 kJ mol^{-1} and 77 kJ mol^{-1} for Kr and 56 kJ mol^{-1} and 108 kJ mol^{-1} for Xe (Fig. 5c, Supplementary Fig. 24 and Supplementary Videos 5 and 6).

All the computed diffusion pathways reveal substantially higher energy barriers for Xe than for Kr, which aligns with the experimental observations and supports a kinetically controlled sieving mechanism. Notably, our CI-NEB calculations reveal that transport is most favorable along the *a*-axis, with Path-a identified as the most energetically favorable trajectory and thus expected to dominate the separation mechanism. Accordingly, it is important to clarify how the cooperative structural flexibility of the succinate linkers facilitates the kinetic-driven separation of Kr from Xe along Path-a. As demonstrated in Supplementary Videos 3 and 4, the migration of Kr and Xe through this path reveals aperture adaptability mediated by the coordinated motions of the succinate linkers. As molecules approach the window, this dual-mode flexibility mechanism, which combines linker displacement and rotational freedom, enables diffusion while preserving framework integrity. During Kr passage, the succinate linkers – which exhibit a dihedral angle of 20.5° between the carboxylate (O-C-O) plane and the aliphatic (C-C-C) plane in the activated MIP-203-Suc structure – are significantly rotated. This distortion increases the same interplanar angle to 34.8°, representing a 14.3° deviation from equilibrium (Fig. 5d–f). The linker twisting effect is more pronounced for Xe, where the angle reaches 40.9°, forcing the linker to sacrifice its preferred geometry to accommodate this bulkier guest molecule

(Supplementary Fig. 25). These rotational motions—clearly visible in Supplementary Videos 3 and 4 — occur synergistically with pore aperture expansion. The characteristic C–C distance separating the opposite aliphatic chain initially measured at 5.6 Å expands to 6.66 Å when Kr crosses. Interestingly, these deformations are fully reversible; evidence lies in the smooth elastic recovery of linkers back to their equilibrium configurations (both in separating distances and dihedral angles) following guest passage.

Furthermore, Raman spectroscopy was applied to monitor the MOF dynamic characteristics before and after loading Kr into the pore structure (Supplementary Fig. 26). Notably, two absorption peaks corresponding to the symmetrical and asymmetrical vibrations of succinate carboxylates exhibited pronounced redshifts—from 1604 and 1468 cm^{-1} in their activated form to 1614 cm^{-1} and 1479 cm^{-1} in their Kr-loaded state. In contrast, a peak related to -CH_2 wagging and C-C-C-C stretching blue-shifted by 8 cm^{-1} (from 1284 to 1276 cm^{-1}) after Kr loading[27]. These three significant shifts in the Raman spectra support that local flexibility within succinate is Kr-assisted and most likely contributes to the migration of Kr throughout the MOF pores.

Importantly, the PXRD pattern of the fully Kr-loaded phase differs from that of the activated empty phase; however, it becomes nearly identical to that observed in the as-synthesized phase (Supplementary Fig. 27). This observation suggests that the MIP-203-Suc structure is reversibly flexible upon exposure to Kr-adsorption or a thermal stimulus. This finding sharply contrasts with the relatively rigid structural behavior of this MOF upon CO_2 adsorption even at high gas pressure[27]. This suggests that the activated MIP-203-Suc structure has a selective framework and linker flexibility in response to Kr, thereby facilitating precise diffusion-driven molecular sieving. Powder refinement of high-resolution PXRD data collected from the Kr-fully loaded sample was performed (Supplementary Fig. 28), resulting in a compelling structural model responsive to adsorbed Kr atoms. The Kr atoms are positioned in proximity to the succinate linkers, with distances between the linker hydrogens and Kr ranging from 3.52 to 3.70 Å. Remarkably, these atoms are located at a significant distance from the terminal hydroxyl groups of the Zr_6 clusters (Supplementary Fig. 29). This spatial configuration optimizes the interatomic distances among adjacent Kr atoms, thereby minimizing repulsive interactions and culminating in a stabilized Kr-loaded structure at ambient temperature.

Discussion

To address the well-documented challenge of separating Kr from Xe at room temperature, we propose a strategy that leverages coordination framework materials characterized by structural dynamics. This approach encompasses both framework flexibility and local flexibility, which together facilitate the generation of optimal pore sizes and shapes. The selected on-purpose MOF enables efficient kinetics-driven separation of Kr over Xe with a high breakthrough selectivity of up to 6.3 for a Kr/Xe mixture with a 50:50 ratio at room temperature, which can be further increased to 10.4 when the concentration of Kr is lowered to 1%, thereby supporting its significant potential for xenon purification and radioactive krypton isotope removal from nuclear exhaust gases. Therefore, our findings may extend beyond Kr/Xe systems to other molecular mixtures comprising components with closely related molecular sizes and shapes that pose challenges for kinetics-driven separation.

Methods

Synthesis of MIP-203-Suc

A mixture of $ZrCl_4$ (233 mg, 1 mmol), succinic acid (500 mg, 4.23 mmol), and formic acid (3.8 mL) was transferred into a Teflon-lined autoclave (25 mL) and heated at 393 K for 72 h. Upon cooling to room temperature, a white powder product designated MIP-203-Suc was obtained. The product was then washed with water and subsequently exchanged with methanol several times for further purification.

Gas adsorption measurement

The as-synthesized MIP-203-Suc samples (minimum of 200 mg) were activated under vacuum at 393 K for 12 h. Single-component gas adsorption and desorption isotherms were measured via a 3Flex instrument (Micromeritics) at various temperatures, specifically, 273 K, 288 K, 298 K, 318 K, 333 K, and 348 K. The pressure range during these measurements ranged from 0 to 100 kPa. Ultrahigh-purity gases (99.999%), including He, N_2, O_2, CO_2, Ar, Xe, and Kr, were utilized in the experiments. To maintain the desired temperatures throughout the process, a Micromeritics ISO Controller (Thermoelectric Cooled Dewar) was employed.

Powder X-ray diffraction analysis

A Bruker D8 Advance powder diffractometer (Cu-Kα, 40 kV and 40 mA) was used to acquire powder X-ray diffraction (PXRD) profiles. The measurement parameters included a scanning speed of 1.0° min^{-1} and a step size of 0.026°.

Synchrotron powder X-ray diffraction analysis

The MIP-203-Suc sample was introduced into a borosilicate glass capillary with an inner diameter of 1 mm. The material underwent activation at 393 K under vacuum for 12 h, after which Kr gas was introduced via a custom-built apparatus. The capillary was subsequently sealed utilizing the flame from a lighter. PXRD data were collected at BL14B1 of the Shanghai Synchrotron Radiation Facility (SSRF), employing a radiation wavelength of 0.6887 Å. For comparative analysis, the synchrotron-radiation XRD patterns were calibrated to the 2θ scale corresponding to Cu-Kα radiation (λ = 1.5406 Å), thereby enabling direct comparison of peak positions with those obtained from laboratory X-ray sources. Structural refinement of the PXRD powder data was conducted via TOPAS software.

Raman spectroscopic analysis

The activated and Kr-loaded MIP-203-Suc samples were prepared via the same methodology employed for synchrotron PXRD analysis. Raman spectra were obtained via a Horiba LabRAM HR Evolution Raman spectrometer, which was equipped with a laser wavelength of 633 nm.

Column breakthrough experiments

Column breakthrough experiments for various gas mixtures were conducted via a custom-designed dynamic breakthrough system. A copper tube with an internal diameter of 5.0 mm and a length of 300 mm was packed with approximately 4.0 g of activated MIP-203-Suc adsorbent. Prior to testing, the column underwent thermal activation at 393 K under vacuum for 12 h and was subsequently pre-saturated with helium. The effluent gas composition was monitored in real time via a Hiden Analytical HPR-20 mass spectrometer. Quantitative analysis of gas purity was performed via a Scion 456-GC gas chromatograph equipped with a PESTEK-MXT-SA-MS PLOT separation column. Following calibration with certified standard gases, component purity values were calculated on the basis of integrated peak areas; specifically, xenon purity was determined through residual subtraction from the krypton concentration data.

DFT calculations

The minimum energy paths (MEPs) for Kr and Xe migration through the triangular apertures of MIP-203-suc were investigated by climbing-image nudged elastic band (CI-NEB) calculations. To map the diffusion pathways, we systematically constructed initial (IS) and final state (FS) configurations by placing individual Kr/Xe atoms outside and inside the pores, respectively. These configurations were DFT geometry-

optimized with fixed experimental cell parameters for the activated MIP-203-Suc sample before CI-NEB calculations.

All the periodic DFT calculations were performed via the Vienna Ab Initio Simulation Package (VASP, version 6.4)[36] with plane-wave basis sets and projector-augmented wave (PAW) potentials[37,38]. The Perdew–Burke–Ernzerhof (PBE)[39] generalized gradient approximation (GGA) was employed with Grimme's empirical dispersion correction (DFT-D3/BJ)[40]. A plane-wave cut-off energy of 600 eV and Γ-point Brillouin zone sampling were used.

For geometry optimizations of the MIP-203-suc and initial/final states (IS/FS) of the Kr/Xe migration paths, convergence criteria of 10^{-6} eV for energy and 0.03 eV/Å for forces were applied. The transition states were located via the VTST module[41] in VASP with the following criteria: 10^{-5} eV and 0.03 eV/Å for the energy and forces, respectively. NEB paths were constructed and analysed via the Atomic Simulation Environment (ASE)[42].

Data availability

All data involved in this work are included in this article and the corresponding supplementary materials. Source data are provided with this paper.

References

1. Franks, N. P., Dickinson, R., de Sousa, S. L. M., Hall, A. C. & Lieb, W. R. How does xenon produce anaesthesia? *Nature* **396**, 324 (1998).
2. Cullen, S. C. & Gross, E. G. The anesthetic properties of Xenon in animals and human beings, with additional observations on Krypton. *Science* **113**, 580–582 (1951).
3. Panda, X. C. et al. Search for light fermionic dark matter absorption on electrons in PandaX-4T. *Phys. Rev. Lett.* **129**, 161804 (2022).
4. Banerjee, D. et al. Metal–organic framework with optimally selective xenon adsorption and separation. *Nat. Commun.* **7**, ncomms11831 (2016).
5. Lipsky, S. R. & Shahin, M. M. Use of Xenon and Krypton as carrier gases for a highly sensitive detection system for gas chromatography. *Nature* **200**, 566–567 (1963).
6. Soelberg, N. R. et al. Radioactive Iodine and Krypton control for nuclear fuel reprocessing facilities. *Sci. Technol. Nucl. Install.* **2013**, 702496 (2013).
7. Kerry, F. G. *Industrial gas handbook: gas separation and purification* (CRC Press, 2007).
8. Banerjee, D. et al. Potential of metal–organic frameworks for separation of Xenon and Krypton. *Acc. Chem. Res.* **48**, 211–219 (2015).
9. Zhang, Z., Ye, Y., Xiang, S. & Chen, B. Exploring multifunctional hydrogen-bonded organic framework materials. *Acc. Chem. Res.* **55**, 3752–3766 (2022).
10. Banerjee, D., Simon, C. M., Elsaidi, S. K., Haranczyk, M. & Thallapally, P. K. Xenon gas separation and storage using metal-organic frameworks. *Chem* **4**, 466–494 (2018).
11. Li, J. R., Kuppler, R. J. & Zhou, H. C. Selective gas adsorption and separation in metal-organic frameworks. *Chem. Soc. Rev.* **38**, 1477–1504 (2009).
12. Gong, W. et al. Programmed polarizability engineering in a cyclen-based cubic Zr(IV) metal–organic framework to boost Xe/Kr separation. *J. Am. Chem. Soc.* **145**, 2679–2689 (2023).
13. Li, L. et al. A robust squarate-based metal–organic framework demonstrates record-high affinity and selectivity for Xenon over Krypton. *J. Am. Chem. Soc.* **141**, 9358–9364 (2019).
14. Pei, J. et al. Robust and radiation-resistant Hofmann-type metal-organic frameworks for record Xenon/Krypton separation. *J. Am. Chem. Soc.* **144**, 3200–3209 (2022).
15. Liu, Y. et al. Hydrogen-bonded metal–nucleobase frameworks for efficient separation of Xenon and Krypton. *Angew. Chem. Int. Ed.* **61**, e202117609 (2022).
16. Yan, Q. et al. A Ni_4O_4-cubane-squarate coordination framework for molecular recognition. *Nat. Commun.* **15**, 9911 (2024).
17. Elsaidi, S. K. et al. Radiation-resistant metal-organic framework enables efficient separation of krypton fission gas from spent nuclear fuel. *Nat. Commun.* **11**, 3103 (2020).
18. Xiong, S. et al. A microporous metal-organic framework with commensurate adsorption and highly selective separation of xenon. *J. Mater. Chem. A.* **6**, 4752–4758 (2018).
19. Mohamed, M. H. et al. Trailblazing Kr/Xe separation: the birth of the first Kr-selective material. *ACS Appl. Mater. Interfaces* **16**, 29364–29373 (2024).
20. Chen, F. et al. The first Kr-selective carbon molecular sieve for inverse adsorption of krypton over xenon at ambient temperature. *Adv. Mater.* **37**, 2409474 (2025).
21. Fernandez, C. A., Liu, J., Thallapally, P. K. & Strachan, D. M. Switching Kr/Xe selectivity with temperature in a metal–organic framework. *J. Am. Chem. Soc.* **134**, 9046–9049 (2012).
22. Wang, H. et al. Crystallizing atomic Xenon in a flexible MOF to probe and understand its temperature-dependent breathing behavior and unusual gas adsorption phenomenon. *J. Am. Chem. Soc.* **142**, 20088–20097 (2020).
23. Kim, H. et al. Switchable Xe/Kr selectivity in a hofmann-type metal–organic framework via temperature-responsive rotational dynamics. *Small* **19**, 2301905 (2023).
24. Xiong, H. et al. Topology reconfiguration of anion-pillared metal–organic framework from flexibility to rigidity for enhanced acetylene separation. *Adv. Mater.* **36**, 2401693 (2024).
25. Parent, L. R. et al. Pore breathing of metal–organic frameworks by environmental transmission electron microscopy. *J. Am. Chem. Soc.* **139**, 13973–13976 (2017).
26. Zeng, H. et al. Orthogonal-array dynamic molecular sieving of propylene/propane mixtures. *Nature* **595**, 542–548 (2021).
27. Wang, S. et al. Engineering structural dynamics of zirconium metal–organic frameworks based on natural C4 linkers. *J. Am. Chem. Soc.* **141**, 17207–17216 (2019).
28. Kang, C. et al. Covalent organic framework atropisomers with multiple gas-triggered structural flexibilities. *Nat. Mater.* **22**, 636–643 (2023).
29. Tian, Y.-J. et al. Pore configuration control in hybrid azolate ultramicroporous frameworks for sieving propylene from propane. *Nat. Chem.* **17**, 141–147 (2025).
30. Huang, Y. et al. Delicate softness in a temperature-responsive porous crystal for accelerated sieving of propylene/propane. *J. Am. Chem. Soc.* **145**, 24425–24432 (2023).
31. Wang, H. et al. Docking of CuI and AgI in metal–organic frameworks for adsorption and separation of xenon. *Angew. Chem. Int. Ed.* **60**, 3417–3421 (2021).
32. Wang, H. et al. The first example of commensurate adsorption of atomic gas in a MOF and effective separation of xenon from other noble gases. *Chem. Sci.* **5**, 620–624 (2014).
33. Huang, J. et al. A microporous hydrogen-bonded organic framework based on hydrogen-bonding tetramers for efficient Xe/Kr separation. *Angew. Chem. Int. Ed.* **62**, e202315987 (2023).
34. Chen, L. et al. Separation of rare gases and chiral molecules by selective binding in porous organic cages. *Nat. Mater.* **13**, 954–960 (2014).
35. Ruthven, D. M. *Principles of adsorption and adsorption processes*. (Wiley, 1984).
36. Kresse, G. & Furthmüller, J. Efficient iterative schemes for ab initio total-energy calculations using a plane-wave basis set. *Phys. Rev. B.* **54**, 11169–11186 (1996).
37. Kresse, G. & Joubert, D. From ultrasoft pseudopotentials to the projector augmented-wave method. *Phys. Rev. B.* **59**, 1758–1775 (1999).

38. Blöchl, P. E. Projector augmented-wave method. *Phys. Rev. B.* **50**, 17953–17979 (1994).
39. Perdew, J. P., Burke, K. & Ernzerhof, M. Generalized gradient approximation made simple. *Phys. Rev. Lett.* **77**, 3865–3868 (1996).
40. Grimme, S., Antony, J., Ehrlich, S. & Krieg, H. A consistent and accurate ab initio parametrization of density functional dispersion correction (DFT-D) for the 94 elements H-Pu. *J. Chem. Phys*. **132**, 154104 (2010).
41. Henkelman G. Vasp TST Tools. Available from: http://theory.cm.utexas.edu/vtsttools/.
42. Hjorth et al. The atomic simulation environment—a Python library for working with atoms. *J. Phys. Condens. Matter* **29**, 273002 (2017).

Acknowledgements

S.D., C.Y., Q.L., S.X., and X.W. acknowledge the funding support of CAEP foundation (CSKS20240050) from China Academy of Engineering Physics. B.Z. and S.W. acknowledge the funding support of the National Natural Science Foundation of China (22071234), the Chinese Academy of Science (XDB1300000), and the CAS Talent Introduction Program (Category B, KJ9990007009). The computational work was performed using HPC resources from GENCI-CINES (Grant A0180907613). G.M. extends his appreciation to Institut Universitaire de France for awarding him a Senior Chair position. The material characterization in this work was partially carried out at the Instruments Centre for Physical Science, University of Science and Technology of China. The authors would like to extend their heartfelt thanks to Dr. Shiming Zhou, Dr. Yinhua Zhao, Dr. Mei Sun, Dr. Jun Zhou, Dr. Wanting Liu, Dr. Duo Zhang, Dr. Boyu Liu, and Dr. Songzhu Qi for their significant contributions and constructive discussions.

Author contributions

Conceptualization, S.W. and S.X.; Investigation, S.D., B.Z., M.W., G.M., C.Y., Q.L., S.X., S.W., and X.W.; Writing-Original Draft, S.W., G.M., and S.X.; Writing-Review & Editing, S.D., B.Z., M.W., G.M., Q.L., S.X., S.W., and X.W.; Supervision, S.W., G.M., S.X., and X.W.

Competing interests

The authors declare no competing interests.

Additional information

Supplementary information The online version contains supplementary material available at https://doi.org/10.1038/s41467-025-67537-3.

Correspondence and requests for materials should be addressed to Shunshun Xiong, Sujing Wang or Xiaolin Wang.

Peer review information *Nature Communications* thanks the anonymous reviewer(s) for their contribution to the peer review of this work. A peer review file is available.